Applied Catalysis B: Environmental 322 (2023) 122137

Contents lists available at ScienceDirect

Applied Catalysis B: Environmental

journal homepage: www.elsevier.com/locate/apcatb

Dual-site activation of H_2 over $Cu/ZnAl_2O_4$ boosting CO_2 hydrogenation to methanol

Lixin Song, Hui Wang, Shuai Wang, Zhenping Qu *

Key Laboratory of Industrial Ecology and Environmental Engineering (Ministry of Education, China), School of Environmental Science and Technology, Dalian University of Technology, Linggong Road 2, Dalian 116024, China

ARTICLE INFO

Keywords:
CO_2 hydrogenation
Dual-site activated H_2
Metal-oxide interface
SMSI
$ZnAl_2O_4$ spinel

ABSTRACT

Methanol synthesis derived from CO_2 hydrogenation has attracted great attention in terms of CO_2 recycling while suffering from the low activity and sintering of copper species. Herein, we unveil the remarkable activity (11.3%) and methanol STY (242 g_{CH3OH} kg_{cat}^{-1} h^{-1}) of 8 wt% $Cu/ZnAl_2O_4$ at 220 °C and 3 MPa, far surpassing that of conventional 8 wt% $Cu/ZnO/Al_2O_3$ composite oxides (6.8% for CO_2 conversion and 144 g_{CH3OH} kg_{cat}^{-1} h^{-1} for methanol STY). The brilliant capability of H_2 dissociation over $Cu/ZnAl_2O_4$ promotes methanol production due to the strong metal-support interaction. In-depth characterization points that the interstitial H atoms in $ZnAl_2O_4$ support contribute to the generation of the formate species, whose hydrogenation to methanol is participated by the H atoms dissociated from Cu nanoparticles. Dual-site activation of H_2 allows an acceleration of methanol synthesis. This work offers a new avenue to modify catalyst structure for effectual CO_2 hydrogenation under moderate conditions.

1. Introduction

Excessive CO_2 emissions exacerbate ecological issues, including global warming and ocean acidification, etc. [1]. As a major waste product of combustion reactions, CO_2 is a safe, non-toxic and economical C1 source [2]. Recently, it has attracted considerable attention in the conversion of CO_2 into essential fuels, including CO [3], CH_4 [4], CH_3OH [5–8], C_2H_5OH [9], HCOOH [10], dimethylether (DME) [11], gasoline [12], olefins [13] and aromatics [14], etc. In particular, methanol can be deployed to store renewable hydrogen energy (H_2, produced by solar energy, hydropower and wind power), and meanwhile it can also serve as a transfer station for further reform into other high value-added chemicals [15]. Nonetheless, there is still tremendous adversity due to the chemical inertness of CO_2 molecules. Accordingly, significant catalytic advances are urgently necessary to drive the process efficiently.

In the past decades, a variety of heterogeneous catalysts, such as Cu/ZnO [16], ZnO-ZrO_2 solid solution [17], In_2O_3 [18], $InNi_3C_{0.5}$ [19], Co/Ce oxides [4], alloy catalysts [20], MOFs [2,21], carbides [22], sulfides [7], etc., have been developed for CO_2 hydrogenation for methanol synthesis reaction. Wherein, Cu/ZnO-based catalysts (e.g., CuZnAl, CuZnZr) are the most extensively explored owing to the high selectivity of methanol and low cost. Plenty of research has uncovered that the synthesis of methanol via CO_2 hydrogenation over Cu-based catalysts is a structure-sensitive reaction [23]. The synergetic effect between copper and support, for instance, strong metal-support interaction (SMSI), defects, steps, etc. [24], seem to play an essential role. Despite great efforts have been made, several problems still exist, including lower activity (usually below 10%) under moderate temperatures (200–250 °C) and rapid deactivation, which is caused by copper sintering due to the high copper loading (20–60 wt%), and the agglomeration of ZnO species as a result of the generated water during CO_2 hydrogenation [25]. However, lowering the amount of Cu means a lack of H_2 activation sites. The addition of precious metals can promote the activation of H_2, but it is restricted by the limited natural abundance [19]. Besides, the activation sites for H_2 in the previous study are predominantly monocentric (such as Cu [23], Zn [26], Pd cluster [27], In [18], etc.), limiting the dissociation of H_2. Constructing the SMSI by the formation of metal-support interfaces would not only supply CO_2 adsorption sites, but also enhance the electron transfer efficiency of metals and supports, promoting the activation of H_2. Consequently, such Zn-rich support is needed urgently, which can avoid ZnO agglomeration, and it is also essential to build the SMSI.

Spinel oxides (AB_2O_4) have gained insight due to abundant surface

* Corresponding author.
E-mail address: quzhenping@dlut.edu.cn (Z. Qu).

https://doi.org/10.1016/j.apcatb.2022.122137
Received 14 July 2022; Received in revised form 17 October 2022; Accepted 31 October 2022
Available online 1 November 2022

active sites, tunable electron exchange abilities and high stability in catalysis [28]. Spinel with a domain-limited structure, which retains metal cations in tetrahedral or octahedral positions, could block the growth of the metal cations [29]. Meanwhile, the exposed polar surface of spinel can anchor the loaded metal particles [30], allowing the formation of the SMSI and hindering the agglomeration of the metal species [31]. Based on the inspiring clue, $ZnAl_2O_4$ spinel may be a potential support. The application of bare $ZnAl_2O_4$ to CO_2 hydrogenation has been trialed [26], however, the CO_2 conversion is unsatisfactory (less than 4%). In addition, there has been some preliminary exploration of $ZnAl_2O_4$ supported copper catalysts for the synthesis of methanol driven by CO_2 hydrogenation. F. Le Peltier et al. [32] studied the reaction kinetics of CO_2-to-methanol over $Cu/ZnAl_2O_4$ catalyst at 250 °C up to 0.3 MPa using in situ FT-IR spectroscopy, pointing out that the hydrogenation of carbonate species to formate species adsorbed on Cu is the rate-determining step. Additionally, the evolution of the intermediate species in the CO_2 hydrogenation reaction over the spinel-type $Cu/ZnAl_2O_4$ catalyst has been developed by M. Huš et al. [24] using the CCSD (T) calculations, who state that the reaction proceeds the formate pathway with the rate-limiting steps of formate hydrogenation to H_2COO and H_2COOH. The contradiction between experiments and theory as well as the absence of performance and mechanism studies under high-pressure conditions urge us to further explore the behaviors of the promising $Cu/ZnAl_2O_4$ catalysts in the CO_2 hydrogenation to methanol reaction.

Herein, we constructed the $Cu/ZnAl_2O_4$ catalyst with low copper loading (4–12 wt%) and the enhanced SMSI between Cu and $ZnAl_2O_4$ for the synthesis of methanol via CO_2 hydrogenation. The 8 wt% $Cu/ZnAl_2O_4$ catalyst shows excellent catalytic performance for CO_2 hydrogenation to methanol (11.3% for CO_2 conversion and 242 $g_{CH3OH}\ kg_{cat}^{-1}\ h^{-1}$ for STY of methanol obtained at 220 °C and 3 MPa). The results indicate that the SMSI between Cu and $ZnAl_2O_4$ is essential to promote CO_2 adsorption and H_2 activation. Meanwhile, the interstitial H atoms in spinel boost the conversion of CO_2 to formate species, while the dissociated H_2 by Cu enhances the hydrogenation of formate to methanol. All in all, the transformation of CO_2 to methanol is accelerated by the metal/spinel catalysts with dual-site superior capacity for dissociation of H_2.

2. Experimental section

2.1. Catalyst preparation

2.1.1. Synthesis of spinel $ZnAl_2O_4$

The synthesized $ZnAl_2O_4$ spinel catalyst was prepared by the co-precipitation method [24] using ammonia solution ($NH_3{\cdot}H_2O$, 25–28%) as the precipitating agent. The detailed procedure was described in the Supporting Information. At last, the $ZnAl_2O_4$ catalyst was labeled as ZA-S.

2.1.2. Synthesis of composite oxide ZnO/Al_2O_3

The traditional ZnO/Al_2O_3 composite catalyst was prepared by Na_2CO_3 coprecipitation [33]. The details were given in the Supporting Information. The ZnO/Al_2O_3 composite oxide was denoted as ZA-C.

2.1.3. Synthesis of $Cu/ZnAl_2O_4$ or $Cu/ZnO/Al_2O_3$

The metal copper was introduced on the support surface by previous wet impregnation [34] using aqueous solutions of copper nitrate. The detailed procedures were well documented in the Supporting Information. The content of copper in ternary catalysts was 4, 6, 8, and 12 wt%, which were identified as X-CZA-S or X-CZA-C (X was used to represent the mass percentage content of the copper loading), respectively.

2.2. Catalyst performance evaluation

The hydrogenation of CO_2 to methanol was conducted in a home-built high-pressure continuous-flow fixed-bed reactor, corresponding evaluation procedure was similar to our previous work [35,36], which was well recorded in the Supporting Information.

2.3. Characterization of the catalysts

The X-ray diffraction (XRD), Scanning electron microscopy (SEM), High-resolution transmission electron microscopy (HRTEM), N_2 adsorption and desorption, H_2 temperature-programmed-reduction (H_2-TPR), N_2O oxidation followed by H_2 titration, X-ray photoelectron spectroscopy (XPS) and CO-IR adsorption experiments were carried out for the characterization of the catalyst structures, and the detailed procedures were noted in the Supporting Information.

2.4. Temperature-programmed desorption experiments

CO_2 or H_2 temperature-programmed desorption (CO_2/H_2-TPD) measurements of the reduced catalysts were carried out on a quadrupole mass spectrometer (QMS, Pfeiffer OmniStar 320) equipped with a computer-interfaced as the detector. Prior to each experiment, the reduced catalysts (0.05 g) went through the pre-treatment amidst the He atmosphere at 200 °C for 30 min to clean the sample surface. After cooling to room temperature, the samples were saturated with pure CO_2 or H_2 at room temperature for 30 min, followed by introducing He to get rid of the weekly physisorbed molecules. Subsequently, the TPD experiment was conducted in flowing He with a ramp rate of 10 °C/min, and the desorbed CO_2 or H_2 data was acquired by the mass spectrometer. The experimental procedure for He-TPD is the same as for H_2-TPD expect for the saturation of H_2 adsorption at room temperature.

2.5. High-pressure in situ DRIFTS experiments

High-pressure in situ diffuse reflectance infrared Fourier transform spectroscopy (in situ DRIFTS) analysis was acquired to evaluate the surface adsorbed species during CO_2 adsorption and hydrogenation. All spectrograms, ranging from 800 to 4000 cm^{-1} at a resolution of 4 cm^{-1}, were documented by VERTEX70 equipped with an FTIR spectrometer and an MCT detector cooled with liquid nitrogen. The catalysts were placed in a ceramic crucible in a stainless-steel cell fitted with ZnSe windows for observation at 220 °C as well as a high-pressure chamber (3 MPa). Correction of the background of the spectra was achieved by subtracting the spectra of the clean wafers at the corresponding temperature. The in situ DRIFT spectra were processed by the OPUS software and expressed in units of Kubelka-Munk. Similar to other characterizations, the pre-reduced catalysts were desired. *In situ* DRIFTS experiment is performed by the following steps: (1) acquisition of background in N_2 condition (3 MPa, 60 mL/min); (2) collection of adsorbed carbon species on the sample surfaces under CO_2/N_2 conditions (3 MPa, 60 mL/min); (3) removal of weakly adsorbing species from sample surfaces by N_2 blow (3 MPa, 60 mL/min); (4) switch to H_2/N_2 mixture for CO_2 hydrogenation (3 MPa, 60 mL/min); (5) exposing to N_2 atmosphere and cool off.

3. Results and discussion

3.1. Catalytic performance for CO_2 hydrogenation

For both the 8-CZA-S and 8-CZA-C catalysts, the former catalyst exhibits superior space-time yield (STY) of methanol at a rate of 242–248 $g_{CH3OH}\ kg_{cat}^{-1}\ h^{-1}$ at 220–260 °C (Fig. 1), approximately 1.7 times higher than that of the latter catalyst (144–141 $g_{CH3OH}\ kg_{cat}^{-1}\ h^{-1}$ in the identical temperature range (220–260 °C). In the case of the conversion of CO_2, it can be discovered that there is an enhancement of about 1.6 times when the support is converted from ZA-C to ZA-S. In particular, CO_2 conversion for 8-CZA-S can reach 11.3% at 220 °C. Despite the gradual decrease in methanol selectivity of both catalysts

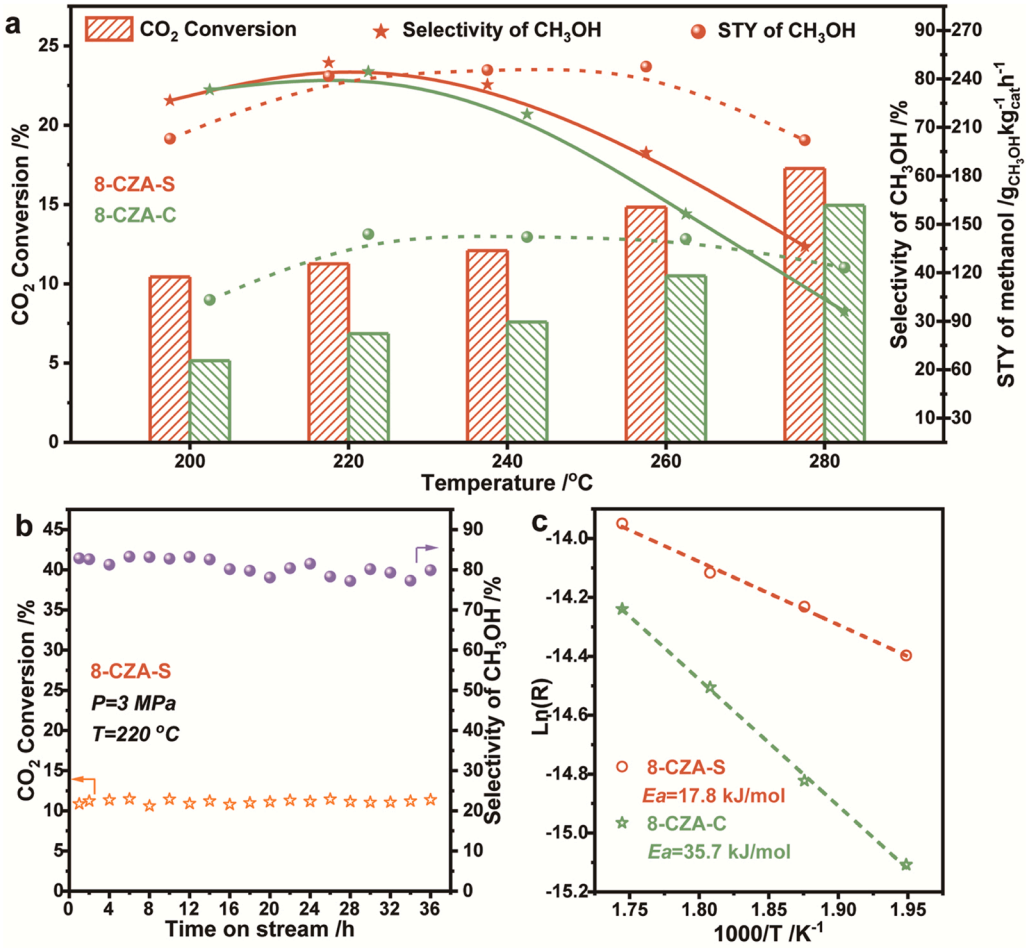

Fig. 1. The catalytic properties in CO_2 hydrogenation to methanol over 8-CZA-S and 8-CZA-C catalysts. a) Catalytic performance. CO_2 conversion (bar), methanol selectivity (star, solid line), and space-time yield (STY) of methanol (sphere, short dash line) as a function of the temperature over 8-CZA-S (tangerine) and 8-CZA-C (green) catalysts. b) Stability test of the 8-CZA-S catalyst. c) Activation energy. Reaction conditions for the catalytic test: GHSV= 9000 h^{-1}, T = 220 °C, CO_2:H_2 = 1:3, P = 3.0 MPa.

with rising temperature, the selectivity of methanol over the 8-CZA-S catalyst is consistently slightly higher than that of the 8-CZA-C catalyst, which is mainly due to the more effective in inhibiting reverse water-gas reactions (RWGS) for 8-CZA-S catalyst (Fig. S1). Thus, the remarkable STY of methanol is the result of significant improvements in CO_2 conversion and dependable selectivity of methanol. In addition, copper loading was also modulated to investigate the methanol synthesis from CO_2 hydrogenation (Fig. S2). The CO_2 conversion, methanol selectivity and STY of methanol exhibit in the volcanic shape, and it reaches a maximum at 8% copper loading. Besides, the long-term stability test of the 8-CZA-S catalyst presents no visible decline in activity and selectivity over 36 h at 220 °C and 3 MPa, with a stable conversion and methanol selectivity of around 11% and 80%, respectively (Fig. 1b).

The kinetic experiments prove that there is a considerable advantage in activation energy for 8-CZA-S (E_a = 17.8 kJ/mol), compared to the other catalysts (Fig. 1c and Fig. S2e). The performance of the 8-CZA-S catalyst is compared with that of copper-containing catalysts reported in the literature (Table S1). Surprisingly, the 8-CZA-S catalyst provides superior STY of methanol among the catalysts with less than 10% copper loading. Despite the fact that the apparent STY of methanol for the 8-CZA-S catalyst is slightly lower than some copper-based catalysts, it is still superior in terms of copper loading and operating conditions. Such superior catalytic properties encourage us to further explore the structure of the 8-CZA-S catalyst and the reaction mechanism in methanol synthesis derived from CO_2.

3.2. Structural features and SMSI effect of the catalysts

3.2.1. Basic structural characteristics of the catalysts

The wide-angle XRD pattern of the ZA-S catalyst displays well-resolved reflections in the 2θ values of 31.3°, 36.8°, 44.8°, 49.0°, 59.2°, and 65.1°, which can be assigned to (220), (311), (400), (331), (511), and (440) lattice planes of the cubic $ZnAl_2O_4$ phase [37], respectively (Fig. 2a). When a certain amount of copper (8 wt%) is introduced to $ZnAl_2O_4$, several small spikes attributed to CuO appear. Meanwhile, the peaks of $ZnAl_2O_4$ remain changeless in spite of the varying amounts of copper (Fig. S3), indicating that the crystalline structure of $ZnAl_2O_4$ has no bearing on the introduction of copper. However, the XRD patterns of the traditional ZA-C or CZA-C catalysts only show peaks attributed to ZnO or/and CuO, which means that Al_2O_3 is present in an amorphous form. With the incorporation of copper, the peaks associated with ZnO become more defined. That is to say that the Cu loading will result in the growth of ZnO [38]. After the reduction of all catalysts in pure H_2, only the metal copper exists in Cu-containing catalysts. Furthermore, the XRD patterns of the spent samples (Fig. S4) were performed to acquire details of structural changes for the catalysts before and after the reaction. It can be found that both supports (spinel and composite oxide) remain stable during the reaction process. Surprisingly, the grain size of the metallic Cu species in the 8-CZA-C catalyst increased after the reaction, while there was little change in that over the 8-CZA-S catalyst. The result indicates a stronger anchoring effect of the spinel towards the Cu species.

The textural information of the catalysts can be obtained from the N_2 adsorption-desorption isotherms. As can be seen from Fig. S5, all the catalysts exhibit the Type-IV adsorption isotherms with a hysteresis loop

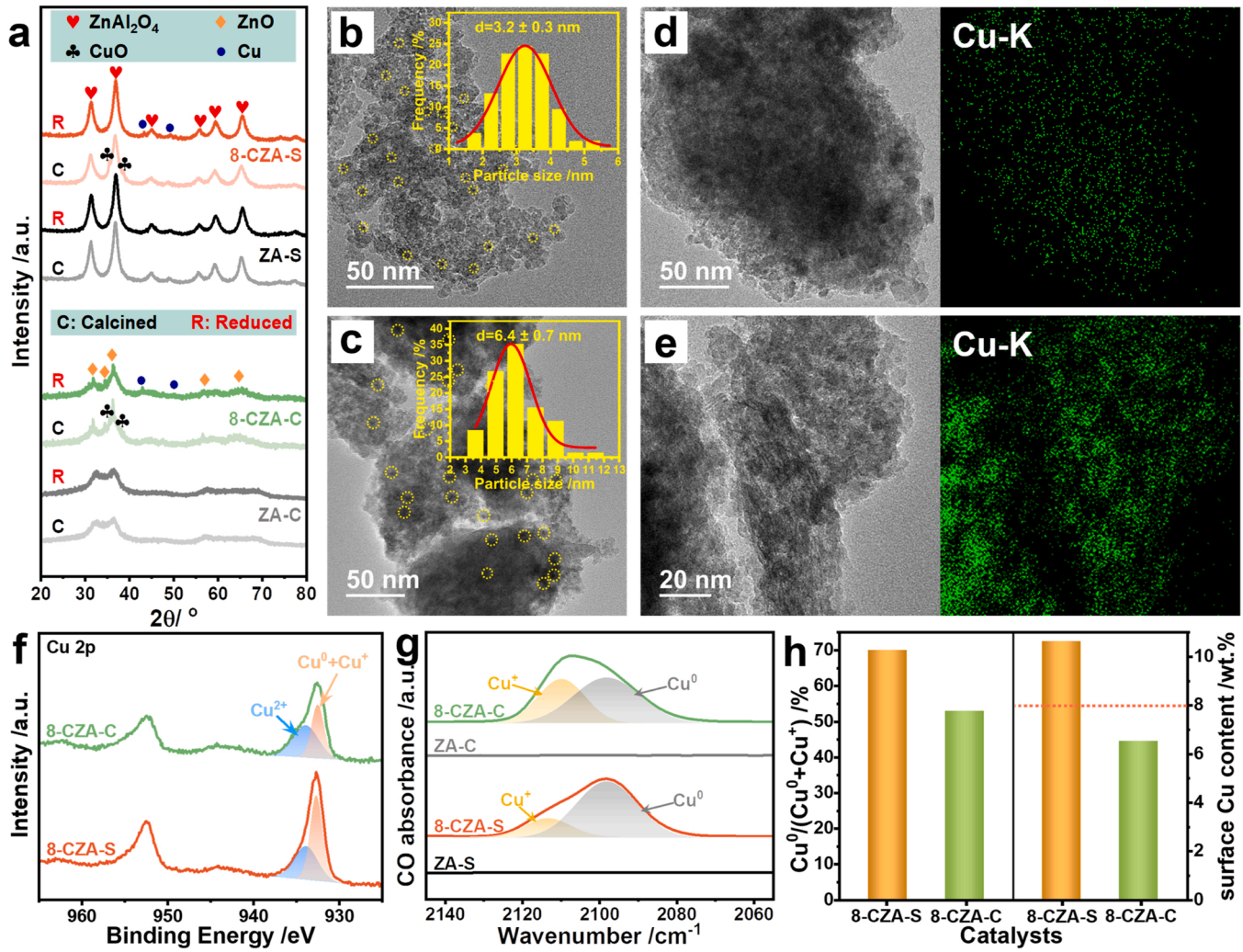

Fig. 2. Identification of the physical phase structure of the catalysts. a) XRD patterns of the catalysts (C: calcined in air, R: reduced in H_2 after calcination). STEM images and the size distribution of Cu particles in the reduced catalysts: b) 8-CZA-S and c) 8-CZA-C. STEM images and corresponding EDX mapping of the reduced catalysts: d) 8-CZA-S and e) 8-CZA-C. f) Cu 2p XPS spectra of the reduced catalysts. g) Infrared spectra obtained after CO adsorption on the reduced samples at 30 °C. h) The ratio of $Cu^0/(Cu^0+Cu^+)$ determined by CO-IR adsorption experiments (left) and the surface Cu content estimated by XPS (right).

of the Type-H4 according to the IUPAC classification [38], characteristic of mesoporous materials with slit-shaped pores. Importantly, there is only a slight change in the specific surface area of the spinel catalysts after loading Cu, from 81.41 (ZA-S) to 76.09 (8-CZA-S) m^2/g, while the composite oxide catalysts show a considerable drop, from 154.17 (ZA-C) to 97.20 (8-CZA-C) m^2/g (Table 1). This remarkable difference may be related to the catalyst morphology. The 8-CZA-S catalyst is composed of pebble-like planes of small irregular particles, whereas 8-CZA-C exhibits agglomerated bulks (Fig. S6). It is clear that the planar shape of $ZnAl_2O_4$ is more favorable for reducing the loss of specific surface area.

Table 1
Textural and structural properties of the reduced catalysts.

Catalysts	S_{BET} (m^2/g)	$S_{Cu}^{[a]}$ (m^2/g)	$D_{Cu}^{[a]}$ (%)
ZA-C	154.17	–	–
8-CZA-C	97.20	87.3	12.9
ZA-S	81.41	–	–
8-CZA-S	76.09	332.2	49.1
4-CZA-S	79.74	390.3	57.7
6-CZA-S	70.89	366.0	54.1
12-CZA-S	75.38	78.5	41.7

[a] Determined by the N_2O chemisorption method (the S_{Cu} is normalized per gram of Cu).

As the key active component of Cu-based catalysts, the particle size, dispersion, and valence distribution of Cu species play a significant role in the performance of methanol synthesis via CO_2 hydrogenation [39]. The scanning transmission electron microscopy (STEM) images (Fig. 2b-c) illustrate that the Cu particles of the 8-CZA-S catalyst are smaller in size (d=3.2 ± 0.3 nm) compared to those of the 8-CZA-C catalyst (d=6.4 ± 0.7 nm). Besides, the dispersion degree of copper species in spinel catalysts (41.7–57.7%) is significantly higher than that of conventional composite oxide catalysts (12.9%) (Table 1 and Fig. 2d-e), despite the well-dispersion of other elements (Zn, Al, and O) on both catalysts (Fig. S7). In addition, the XPS spectra give the evidence that the dominant Cu species on the surface of both the 8-CZA-S and 8-CZA-C catalysts are present in the form of Cu^0 and Cu^+ (Fig. 2 f). However, the ratios of Cu^0 (2098 cm^{-1}) and Cu^+ (2114 cm^{-1}) [40–43] are distinctively different on both catalysts (8-CZA-S and 8-CZA-C) from IR experiments for CO adsorption (Fig. 2g-h). It is very clear that the 8-CZA-S catalyst has higher Cu^0 amount (39.63%), compared against the 8-CZA-C catalyst (23.15%) (Table S2). Analogously, the distinction between Cu^0 and Cu^+ was also discriminated over the reduced X-CZA-S catalysts (Fig. S8). It is quite intuitive that the share of Cu^0 on the spinel catalysts is higher than that on the composite oxide sample, regardless of the Cu loading. Cu^0 species seem to serve an irreplaceable role in the

present study. Furthermore, the higher surface copper content of the 8-CZA-S catalyst (10.64 wt%, Fig. 2 h) indicates that the copper species are more susceptible to be enriched on the surface of spinel.

3.2.2. Identification of the SMSI for the catalysts

The SMSI between Cu and supports was first explored by the HRTEM technique, with the images displayed in Fig. 3a-b. In the lattice stripe region of the 8-CZA-S catalyst, the measured distances between two parallel lattice stripes are 0.209, 0.181, 0.286, 0.244, and 0.143 nm, corresponding to the (111) and (200) crystal plane of Cu and the (220), (311), and (440) crystal planes of $ZnAl_2O_4$, respectively. The results show a high consistency with the SAED images (Fig. S9a) and XRD patterns (Fig. 2a). Unexpectedly, some new lattice stripes (Fig. 3a, d=0.226 nm, d=0.183 nm) are observed within the yellow dashed border. It is reasonable to speculate that nascent lattice streaks are generated by lattice distortion [44–46] due to the strong interaction between Cu and $ZnAl_2O_4$, which is referred to as the Cu-$ZnAl_2O_4$ interface. Likewise, in the case of the lattice stripe region for the 8-CZA-C catalyst, the measured lattice spacings of 0.281 nm and 0.247 nm are attributed to the (100) and (101) crystal plane of ZnO (Fig. 3b), respectively. The results are also confirmed by the XRD patterns (Fig. 2a) and the SAED image (Fig. S9b). However, only slight lattice disturbances can be detected in the contact region between Cu and ZnO (inside the yellow dashed line), perhaps owing to the weak interaction between Cu and the support.

It has been known that the electron mobility of the catalysts with SMSI would be enhanced [19], which could be shown in the form of better redox properties and higher electron binding energy etc. To further confirm the SMSI between Cu and supports, the catalysts were investigated by the H_2-TPR experiments. Surprisingly, the reduction temperature of CuO species over 8-CZA-S is much lower compared to 8-CZA-C (Fig. 3c), proving the stronger metal-support interaction (SMSI) on the 8-CZA-S catalyst [38]. A similar conclusion was obtained by Y. Zhu et al. [47], where the lowest reduction temperature of the Cu/ZrO_2 catalyst demonstrated the strongest MSI between Cu and ZrO_2 among the three catalysts (Cu/SiO_2, Cu/Al_2O_3, and Cu/ZrO_2). The direct evidence for the speculation is also given by the enlarged Cu 2p XPS spectra (Fig. S10). The higher Cu 2p binding energy reflected in the 8-CZA-S catalyst points to the stronger Cu-support interaction for the 8-CZA-S catalyst [19]. Additionally, the SMSI also contributes to the formation of well-dispersed Cu species with small sizes [48]. Two hydrogen consumption peaks in H_2-TPR are observed (Fig. 3c-d). The α peak is ascribed to the highly dispersed CuO species with small crystallite on the catalyst surface. The β peak is assigned to the reduction of CuO species in bulk with large crystallite [49]. Obviously, the larger total H_2 consumption and the higher ratio of α peak area to the total area over the 8-CZA-S catalyst were noticeable in comparison to the 8-CZA-C catalyst, implying more reducible well-dispersed CuO with small crystallite is located on the surface of the 8-CZA-S catalyst. This result reconfirms the stronger MSI on the 8-CZA-S catalyst, which is consistent with the STEM images (Fig. 2b-e). Furthermore, the strength of the SMSI between Cu and $ZnAl_2O_4$ could be modulated by the amount of Cu loading. The α peak in the H_2-TPR profiles shifts towards lower temperatures and then moves up to higher temperatures as the amount of Cu increases (Fig. S11a), pointing to an enhancement and then weakening of the strength of the interaction between Cu and $ZnAl_2O_4$. Similarly, the amount of well-dispersed Cu species with small sizes will be altered with the intensity of the SMSI. The amount of small-sized CuO with fine dispersion gradually grows (4, 6, 8-CZA-S) and subsequently drops (12-CZA-S) due to the aggregation of copper species, which illustrates the remarkable role of the SMSI between Cu and $ZnAl_2O_4$ in regulating the size and dispersion of Cu species. Astonishingly, not only does the 8-CZA-S catalyst have the largest amount of small-sized CuO with fine dispersion, but also the strongest SMSI has been revealed on the 8-CZA-S catalyst among all catalysts.

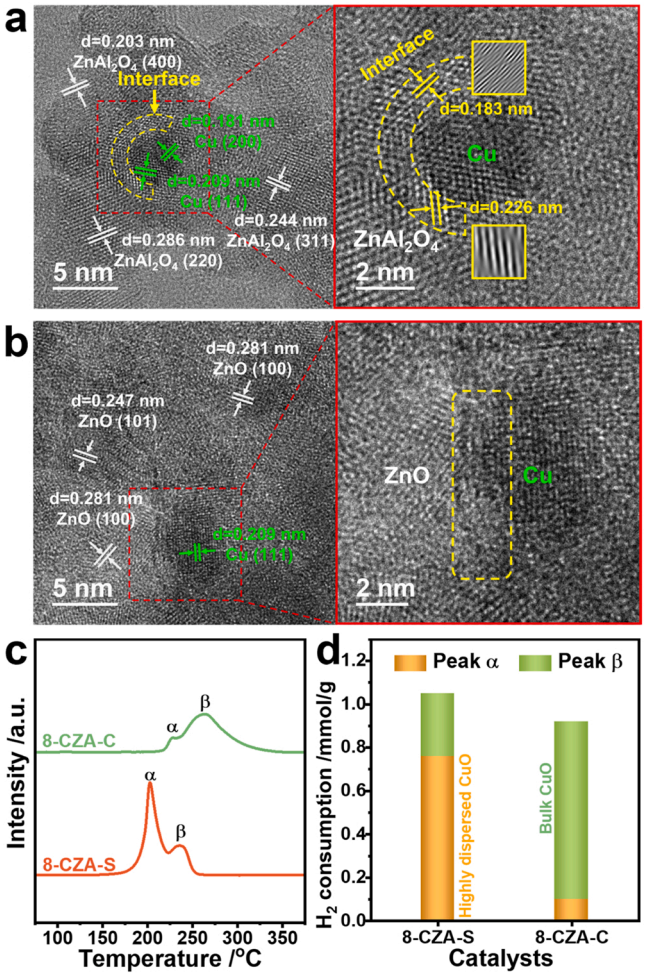

Fig. 3. Identification of the SMSI of the catalysts. Aberration-corrected HRTEM images over the reduced catalysts: a) 8-CZA-S and b) 8-CZA-C. c) H_2-TPR profiles and d) the corresponding H_2 consumption over the calcined catalysts.

In addition, there is also a close relationship between oxygen vacancies and SMSI. The generation of oxygen vacancies can be boosted by employing H_2 as the pretreatment atmosphere, and a possible mechanism for that is the electrons injection from the reductive reagent (H_2) into the d orbitals of the metals, which can vigorously weaken the metal-O bond [50]. The enhancement of electron mobility due to SMSI allows oxygen species to be removed more susceptibly and thereby generating more oxygen vacancies [51]. On the alternative perspective, metal oxides with oxygen vacancies can trap electrons at vacancy centers and modulate the electronic states of as-anchored metal nanoparticles, thus strengthening the SMSI effect [19,52]. The more pronounced increase in the oxygen vacancies for spinel catalysts when copper is intervening on supports (Fig. S12) further gives the evidence of the SMSI between Cu and $ZnAl_2O_4$. The SMSI effect will also be further enhanced by the freshly formed oxygen vacancies.

In brief, the metal-support interfaces derived from the SMSI of the 8-CZA-S catalyst are beneficial for CO_2 hydrogenation to methanol, i.e. providing the adsorption or reaction sites, facilitating the effect of hydrogen spillover [53], etc. Indispensable, the well-dispersed Cu species with small sizes are conducive to the dissociation of hydrogen. These advantageous structural features of the 8-CZA-S catalyst are the foundation for the superior performance of the CO_2-to-methanol reaction.

3.2.3. Dependence of adsorption capability on the SMSI

The capability of adsorbing the reactants CO_2/H_2, determined by CO_2/H_2-TPD measurements, is an essential parameter in the

performance evaluation of catalysts (Fig. 4a-d, Fig. S13, and Table S3). The CO_2 adsorption regions are divided into two main sections. The front peaks (α, 50–250 °C) mark the CO_2 adsorption sites on the support, and the latter peaks (β, 250–350 °C) are associated with the formation of the metal-support interface [54]. It can be found that upon the introduction of copper, the peaks of CO_2 desorption at lower temperature (α) are shifted towards higher temperatures, indicating that the strength of CO_2 adsorption has been reinforced over both catalysts (8-CZA-S and 8-CZA-C). However, there is a significant increase in the α-peak area of the spinel catalysts compared to a slight decrease in that of the composite oxide catalysts (Fig. 4b and Table S3), which should be related with the stronger MSI between Cu and $ZnAl_2O_4$. In addition, the peak β can be observed on the Cu-containing samples compared to the pure supports (Fig. 4a), implying that the Cu-support interface is formed over the both 8-CZA-S and 8-CZA-C catalysts. Nevertheless, a larger β-peak area is obtained for the 8-CZA-S catalyst (Fig. 4b), reflecting a larger metal-support interface is present over that, which is attributed to the highly dispersed Cu species [55]. In parallel, the variation in temperature and area of the α-peak with Cu loading illustrates the regulation of the CO_2 adsorption capacity of the catalyst by the SMSI effect, matching the H_2-TPR results (Fig. S11). Similarly, the change of peak β area shows a volcanic shape (Fig. S13b), which means that the largest Cu-$ZnAl_2O_4$ interface is constructed on the 8-CZA-S catalyst.

Two peaks can be seen in H_2-TPD profiles (Fig. 4c-d) owing to the

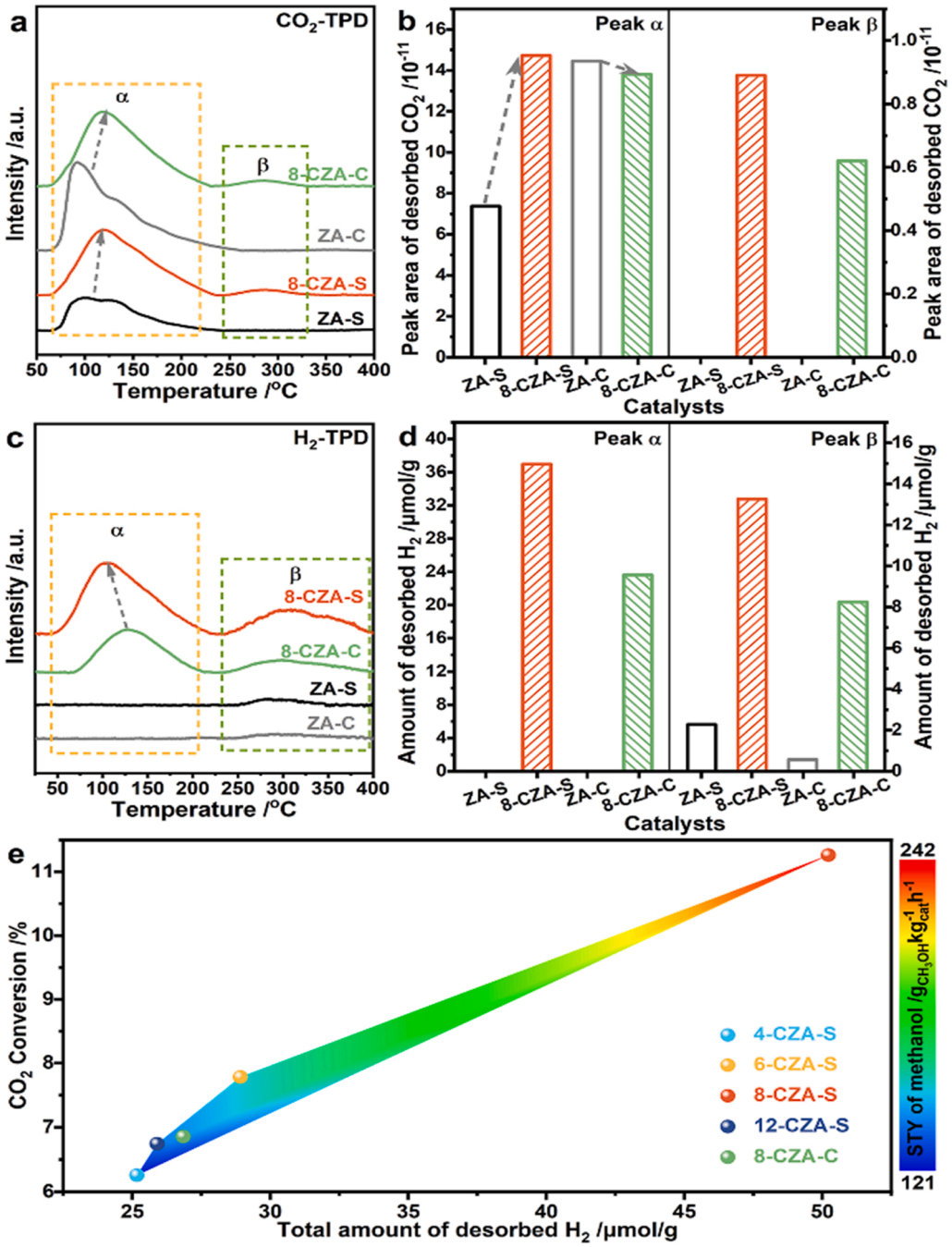

Fig. 4. a) CO_2-TPD profiles and b) the corresponding amount of CO_2 desorption over the reduced catalysts. c) H_2-TPD profiles and d) the corresponding amount of H_2 desorption over the reduced catalysts. e) The relationship between CO_2 conversion and/or STY of CH_3OH (220 °C) and the total amount of desorbed H_2 over the reduced catalysts.

different adsorption states of the hydrogen constituents on the reduced catalyst surface. The former desorption peaks (α) at ca. 100–130 °C originate from the desorption of atomic hydrogen on Cu^0. Whilst, the latter peaks (β) at ca. 300 °C stem from the hydrogen on the $ZnAl_2O_4$ or ZnO/Al_2O_3 surface [56]. It is noticed that the ZA-S support has a certain adsorption capacity for H_2 (2.28 μmol/g) compared with the ZA-C support (0.57 μmol/g) (Fig. 4d and Table S3). The lower temperature and larger area appear in the 8-CZA-S catalyst with respect to the α peak, compared to the 8-CZA-C catalyst, which benefits from the higher Cu^0 concentration and higher exposed copper surface area on the surface. Although the β peak areas of both catalysts are enhanced relative to the supports inherently due to the hydrogen overflow effect, the enhancement is more pronounced for the 8-CZA-S catalyst, which is presumably owing to the stronger MSI and the intensification of hydrogen spillover effects. Simultaneously, it is very unexpected to notice that the position and area of the peak α in H_2-TPD display a similar trend as those of the peak α of H_2-TPR over X-CZA-S catalysts (Fig. S11a and Fig. S13c). In addition, in terms of the peak β, the area gradually decreases with an increase in copper loading, which may be due to the decrease in copper dispersion (Table 1) and the attenuated hydrogen spillover effect. These results reveal the strong dependence of the H_2 adsorption capacity of the catalysts on the SMSI effect.

Examining the relationship between H_2 activation and CO_2 conversion and/or STY of methanol, it is exciting to discover that higher H_2 dissociation ability contributes to the higher CO_2 conversion and STY of methanol (Fig. 4e). Similar conclusions, an excellent positive correlation between CO_2 conversion and the total amount of desorbed H_2, have also been reported by Shi et al. [20]. Given the above analysis, the enhanced electron transfer properties evoked by SMSI facilitate the dispersion and anchoring of copper on $ZnAl_2O_4$ spinel, which contributes to the dissociation of H_2. What matters is that the superior H_2 dissociation capacity of the 8-CZA-S catalyst could motivate the positive shift of the reaction equilibrium, thereby improving the conversion of CO_2 and methanol yield.

3.3. Mechanism study for CO_2 hydrogenation to methanol

3.3.1. Evolution of intermediate species of CO_2 adsorption

To further clarify the evolution of the intermediate species, in situ DRIFT spectra were obtained during CO_2 adsorption (Fig. 5a-d and Table S4). The species of carbonate, formate, and bicarbonate are generated over the ZA-S and 8-CZA-S samples after exposure to CO_2. It is noteworthy that the position of the formate vibrational peak is red-shifted from 1614 to 1608 cm^{-1} after loading copper on ZA-S supports, indicating that some new CO_2 adsorption sites are created at the metal-support interface [57]. Differently, the strong bands of carbonate and bicarbonate are observed over ZA-C and 8-CZA-C catalysts, and the dominant adsorption sites always remain on the ZA-C support surface. Moreover, the strongest adsorption of the intermediate species on the 8-CZA-S catalyst is observed among all catalysts (Fig. 5e). Besides, the intensity of intermediate species over the 8-CZA-C catalyst is slightly weaker than that over the ZA-C catalyst, which is consistent with the CO_2-TPD results (Fig. 4a-b). Furthermore, CO_2-TPD experiments carried out under the reaction conditions (220 °C, 3 MPa) also demonstrate that the CO_2 adsorption capacity of the 8-CZA-S catalyst is larger than that of the 8-CZA-C catalyst (Fig. S14).

It is well recognized that the formation of bicarbonate is related to the hydroxyl species adsorbed on the surface of the catalysts. However,

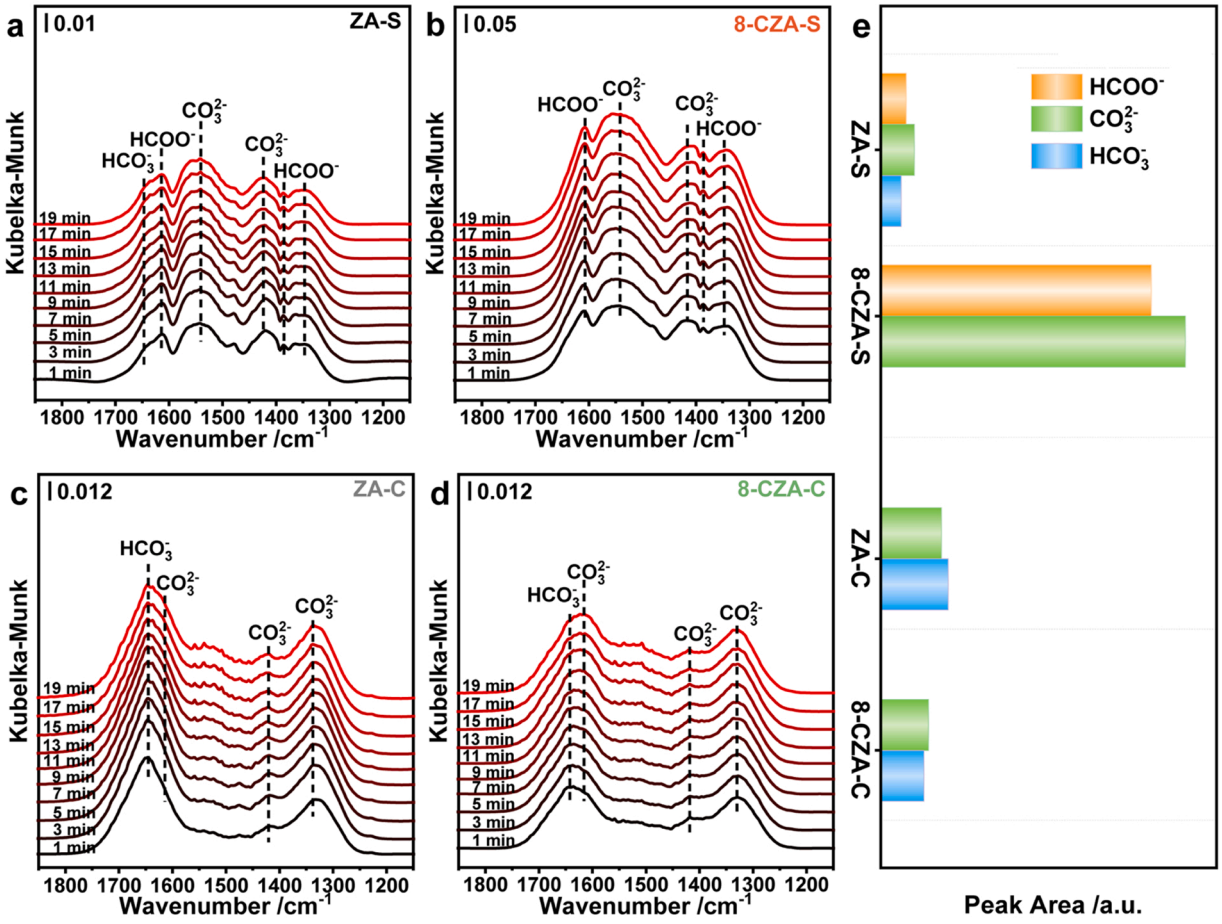

Fig. 5. *In situ* DRIFT spectra of CO_2 adsorption on the reduced catalysts at 3 MPa and 220 °C: a) ZA-S; b) 8-CZA-S; c) ZA-C; d) 8-CZA-C; e) comparison of intermediate species after CO_2 adsorption for 20 min over different catalysts.

there is no detailed research on the origin of hydrogen in formate generation by CO_2 adsorption. To uncover the genesis of the hydrogen, the infrared signal was collected from the calcined ZA-S sample exposed to the CO_2 atmosphere under reaction conditions without H_2 pre-reduction. It can be discovered that no generation of formate is observed under the condition, and only carbonate and bicarbonate are formed (Fig. 6a). The production of formate is seen only after the further introduction of H_2 (Fig. 6b). Consequently, it is reasonable to think that the observation of formate in the ZA-S and 8-CZA-S catalysts (Fig. 5a-b) should be due to the existence of the interstitial H atoms in samples after H_2 reduction (Fig. 6d). Furthermore, when H_2 is pre-adsorbed on the calcined ZA-S catalyst (220 °C, 3 MPa), the formate species can still be detected after the injection of CO_2 gas (Fig. 6c), indicating that hydrogen can be activated by the $ZnAl_2O_4$ support to form interstitial H, retained on the catalyst. Thus, it could be concluded that the interstitial H can facilitate the transformation of carbon-containing species to formate species and be supplemented in the reaction atmosphere (CO_2 +3 H_2, 220 °C, 3 MPa). The substantial increase in the amount of formate species upon loading of Cu onto the spinel support (Fig. 5e) suggests that more interstitial H atoms are produced due to SMSI. Besides, the formation of formate and carbonate species was still detected when the spent 8-CZA-S catalyst was re-exposed to the CO_2 atmosphere (Fig. S15), indicating the structural stability and the potential capability for storing interstitial H of the Cu/$ZnAl_2O_4$ catalyst. Furthermore, the amount of formate and interstitial H-atoms can be tuned by varying the loading of Cu due to the different strengths of SMSI (Fig. S16). The most abundant formate species are observed over the 8-CZA-S catalysts owing to the strongest Cu-$ZnAl_2O_4$ interactions, which is consistent with the H_2-TPR (Fig. S11) and H_2-TPD (Fig. S13c-d) results. According to the above discussion, it can be assumed that the spinel structure is a prerequisite for the formation of formate, and the incorporation of copper enhances the ability to generate interstitial H atoms over the catalysts, further facilitating the formation of formate during the CO_2 adsorption process.

3.3.2. *Hydrogenation processes for CO_2 adsorbed species*

To investigate the reaction of C-containing species with H_2 to generate methanol in detail, H_2 was introduced into the in situ high-pressure DRIFT system after CO_2 adsorption, along with monitoring changes in the species (Fig. 7 and Fig. S17). For ZA-S and 8-CZA-S catalysts (Fig. 7a-b), some fresh vibrational peaks emerge upon the introduction of H_2, including bicarbonate, formate, methoxyl, methanol and methane. It can be noticeable that the carbonates on both catalysts are gradually consumed to generate bicarbonate, formate, and the subsequent hydrogenation products (methanol or methane). In terms of intermediate species contents, the amount of that over the 8-CZA-S catalyst is approximately 10-fold than that over the ZA-S catalyst. Importantly, the rates of consumption and production are distinctly different. For the ZA-S catalyst, only about 20% of the initial amount of

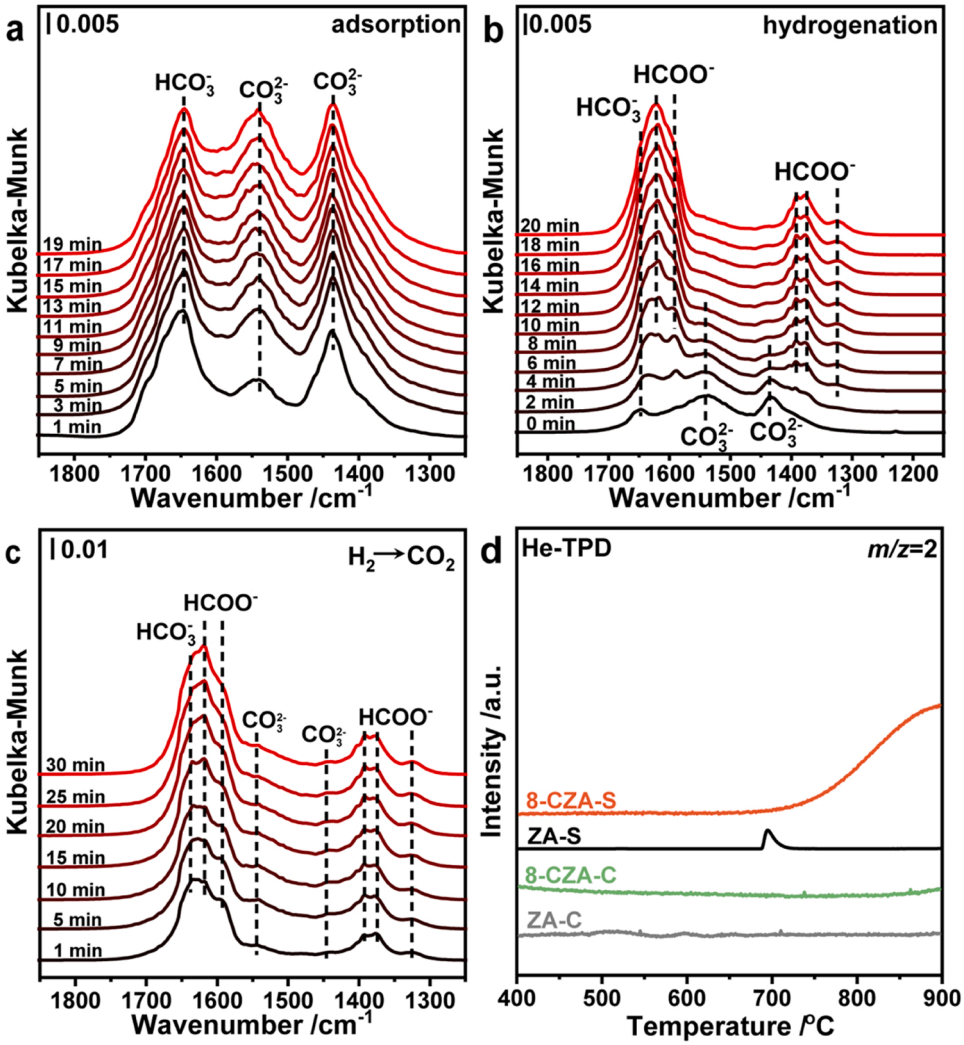

Fig. 6. Recognition of H sources of formate. *In situ* DRIFT spectra over the calcined ZA-S catalysts at 3 MPa and 220 °C: a) CO_2 adsorption; b) hydrogenation process for adsorbed CO_2 species; c) CO_2 adsorption process after pre-adsorption of H_2. d) He-TPD profiles of the reduced catalysts.

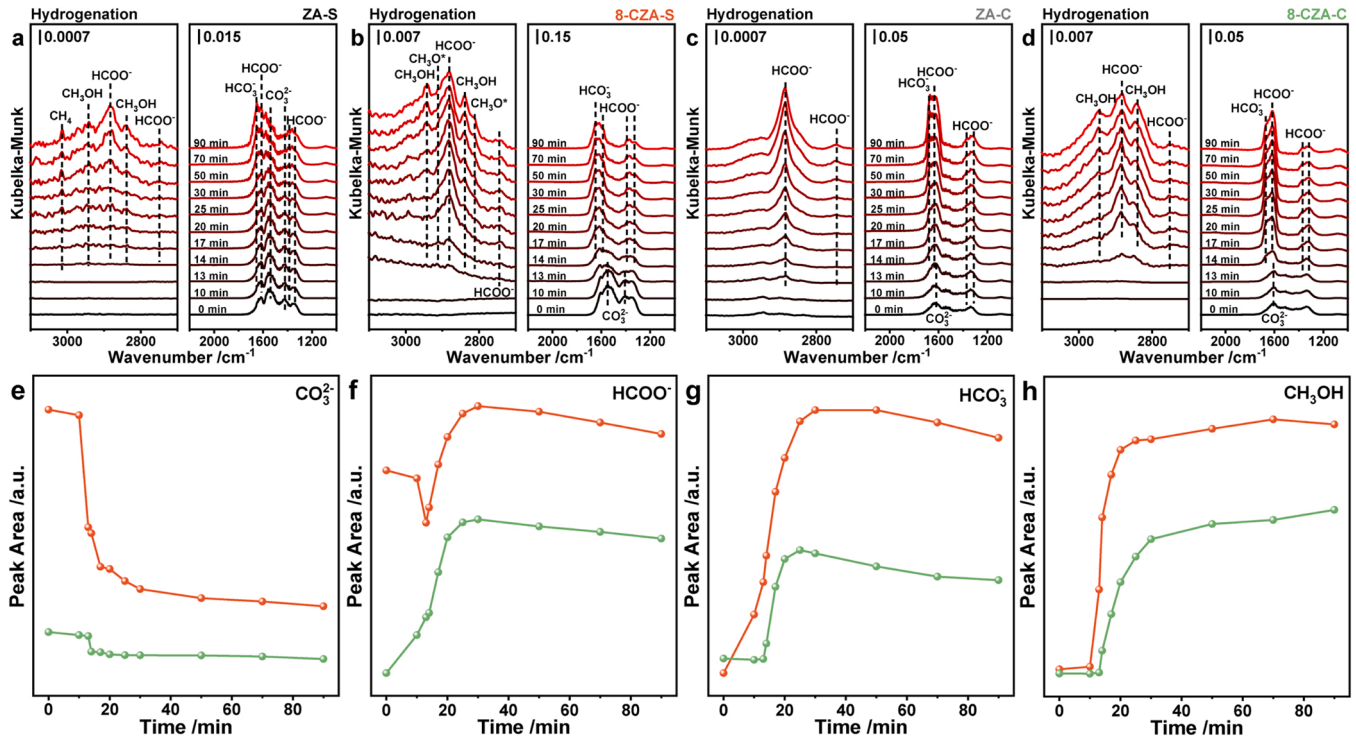

Fig. 7. *In situ* DRIFT spectra of hydrogenation processes for CO_2 adsorbed species over the reduced catalysts at 3 MPa and 220 °C: a) ZA-S; b) 8-CZA-S; c) ZA-C; d) 8-CZA-C. The evolution of the integrated peak area of the characteristic species over time during hydrogenation processes: e) CO_3^{2-}; f) $HCOO^-$; g) HCO_3^-; h) CH_3OH. Herein, the tangerine line: 8-CZA-S and the green line: 8-CZA-C, respectively.

carbonate is consumed after 70 min and the process is relatively slow, whereas 70% of that can be rapidly utilized over the 8-CZA-S catalyst to convert to formate and methanol in 30 min (Fig. S17a-b). The high H_2 dissociation ability in presence of copper induces the fast consumption of intermediate species. The position redshift of the formate over 8-CZA-S catalyst from 1350, and 1384 cm^{-1} to 1338, 1374 cm^{-1} potentially implies a transfer of the reactive center from the support surface to the Cu-support interface.

Similarly, in the case of ZA-C and 8-CZA-C catalysts (Fig. 7c-d), the introduction of H_2 induces the transfer of carbonate to bicarbonate and formate, which could be further hydrogenated to methanol. Unfortunately, only the accumulation of bicarbonate and formate was detected with the carbonates being depleted on the ZA-C catalyst, probably as a consequence of the weak dissociation ability of H_2 (Fig. 4c). In contrast, a little methanol production can still be observed over the ZA-S sample (Fig. 7a) due to the hydrogen activation capability of the ZA-S support (Fig. 4c-d). Similarly, the process of converting carbonate to bicarbonate and formate is accelerated in the presence of copper for the 8-CZA-C catalyst, enabling further hydrogenation to methanol. The above observation reinforces the importance of copper for the dissociation of H_2 in the hydrogenation of CO_2 to methanol.

In comparison with both 8-CZA-S and 8-CZA-C catalysts, it can be realized that the consumption of carbonate species is different. There is just about 25% of the carbonate remains on the 8-CZA-S catalyst after 90 min, as opposed to nearly 40% of that left for the 8-CZA-C catalyst (Fig. 7e and Fig. S17b, d). Meanwhile, the formate species, accumulated during the CO_2 adsorption process due to the presence of interstitial H atoms, will be utilized before accumulation and consumption over the 8-CZA-S catalyst. Whereas, only the processes of accumulation and consumption are presented for formate species over the 8-CZA-C catalyst (Fig. 7f). Besides, a greater amount of hydrogenated intermediate species (formate and bicarbonate) is observed over the 8-CZA-S catalyst, as a result of the stronger ability to dehydrogenate compared to those of the 8-CZA-C catalyst (Fig. 7f-g). Furthermore, the rate and total amount of methanol formation present different results. A considerable amount of methanol can be generated rapidly on 8-CZA-S catalyst relative to 8-CZA-C, with an approximately 1.5-fold increase in terms of methanol (Fig. 7h). The identical results could be obtained in high-pressure in situ mass spectrometry experiments (Fig. S18), which is in accordance with the performance results (Fig. 1a). The vibrational peaks at around 1417 cm^{-1}, attributed to mono-, bi- or polydentate carbonates, still have residues after 90 min during hydrogenation (Fig. 7 and S17). There may be two possible reasons for this phenomenon, either the inadequate hydrogenation capacity of the catalysts or the presence of polydentate carbonate which cannot be removed in the hydrogenation process [58].

3.3.3. *Probable pathways for CO_2 hydrogenation to methanol*

Usually, there are four main reaction mechanisms for the CO_2 hydrogenation reaction to methanol: (1) The HCOO mechanism; (2) The revised HCOO mechanism; (3) The RWGS + CO-Hydro mechanism and (4) The trans-COOH mechanism [39]. In the present study, it has been explored for the evolution of intermediate species in the process of CO_2 adsorption and hydrogenation by high pressure in situ DRIFTS. In the case of the 8-CZA-S catalyst, carbonate and formate were generated during the CO_2 adsorption process (Fig. 5b). Upon switching to the H_2 atmosphere, the original formate species were rapidly consumed to generate methanol (0–13 min, Fig. S17b). Simultaneously, the carbonate was converted with a continuous accumulation of bicarbonates and formates (13–30 min). The overall amounts of bicarbonates and formats begin to decline after 30 min since the rate of production for those is slower than that of consumption. The whole process is accompanied by the formation of methanol. In turn, for the 8-CZA-C catalyst, only the formation of carbonate and bicarbonate is observed during CO_2 adsorption (Fig. 5d). Following the introduction of H_2 (Fig. S17d), the carbonate is consumed. The following accumulation (0–25 min) and consumption (25–90 min) of formate and bicarbonate are observed together with the uninterrupted generation of methanol. In combination with the above results, it can be speculated that both 8-CZA-S and 8-CZA-C catalysts track the formate mechanism since only formate buildup and consumption could be observed (Scheme 1). The only

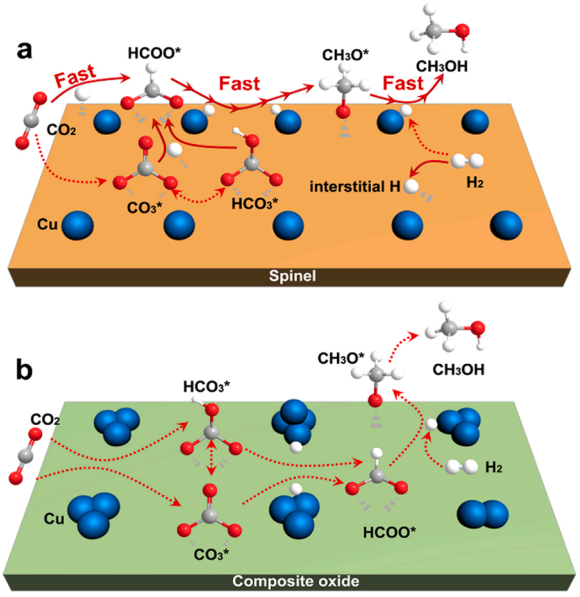

Scheme 1. Reaction pathway for CO_2 hydrogenation to methanol over a) the 8-CZA-S and b) the 8-CZA-C catalysts.

observation of either formate or methoxy indicates that the corresponding C-O bond dissociation of dioxomethylene or the hydrogenation of formaldehyde can be completed instantaneously. Hence, the hydrogenation of formate or methoxy is claimed as the rate-determining step. Conclusively, high-pressure in situ DRIFT experiments demonstrate the superior adsorption of CO_2 and enhanced dissociation capacity for H_2 over the 8-CZA-S catalyst. The dual-site activation of H_2 promotes the performance of CO_2 hydrogenation to methanol. The interstitial H atoms in the spinel contribute to the conversion of the carbonate or bicarbonate to formate species and H atoms activated by Cu facilitate the further hydrogenation of the formate (Scheme 1).

4. Conclusions

In conclusion, the catalysis behavior of Cu anchored by the $ZnAl_2O_4$ spinel support has been investigated for methanol synthesis from direct CO_2 hydrogenation. The conversion of CO_2 and methanol yield over the 8-CZA-S are improved nearly 1.7-fold compared with that over the traditional $Cu/ZnO/Al_2O_3$ composite catalyst (8-CZA-C), reaching 11.3% for CO_2 conversion and 242 $g_{CH3OH}\ kg_{cat}^{-1}\ h^{-1}$ for STY of methanol at 220 °C and 3 MPa respectively. The performance of the 8-CZA-S catalyst could rank in the upper reaches of alternative catalysts with comparable copper loading. The formed $Cu\text{-}ZnAl_2O_4$ interface will supply the abundant CO_2 adsorption sites. Simultaneously, the enrichment of copper on the spinel surface with fine dispersion due to the SMSI further enhances the dissociation of H_2, driving a positive shift in the reaction equilibrium. Furthermore, the interstitial hydrogen atoms in spinel boost the generation of formate species, while the hydrogen atoms dissociated from Cu facilitate the hydrogenation of formate to methanol. Dual-site dissociation of H_2 leads to accelerated production of methanol. A new perspective is proposed for improving the performance of CO_2 hydrogenation to methanol.

CRediT authorship contribution statement

Lixin Song: Conceptualization, Data curation, Formal analysis, Investigation, Methodology, Software, Validation, Visualization, Writing – original draft. **Hui Wang:** Methodology, Validation, Visualization. **Shuai Wang:** Investigation, Software, Visualization. **Zhenping Qu:** Funding acquisition, Project administration, Resources, Supervision, Validation, Writing – review & editing.

Declaration of Competing Interest

The authors declare that they have no known competing financial interests or personal relationships that could have appeared to influence the work reported in this paper.

Data availability

The authors are unable or have chosen not to specify which data has been used.

Acknowledgments

This work was supported by the National Key Research and Development Program of China (No. 2019YFC1903903), the National Natural Science Foundation of China (No. 21876019), the Natural Science Foundation of Liaoning Province (2020-BS-056) and the Fund of the State Key Laboratory of Catalysis in DICP (No. N-18–08).

Appendix A. Supporting information

Supplementary data associated with this article can be found in the online version at doi:10.1016/j.apcatb.2022.122137.

References

[1] S.T. Bai, G. De Smet, Y. Liao, R. Sun, C. Zhou, M. Beller, B.U.W. Maes, B.F. Sels, Homogeneous and heterogeneous catalysts for hydrogenation of CO_2 to methanol under mild conditions, Chem. Soc. Rev. 50 (2021) 4259–4298, https://doi.org/10.1039/d0cs01331e.
[2] A. Modak, A. Ghosh, A. Bhaumik, B. Chowdhury, CO_2 hydrogenation over functional nanoporous polymers and metal-organic frameworks, Adv. Colloid Interface Sci. 290 (2021), 102349, https://doi.org/10.1016/j.cis.2020.102349.
[3] C. Liu, S.L. Nauert, M.A. Alsina, D. Wang, A. Grant, K. He, E. Weitz, M. Nolan, K. A. Gray, J.M. Notestein, Role of surface reconstruction on Cu/TiO_2 nanotubes for CO_2 conversion, Appl. Catal. B 255 (2019), 117754, https://doi.org/10.1016/j.apcatb.2019.117754.
[4] A. Parastaev, V. Muravev, E. Huertas Osta, A.J.F. van Hoof, T.F. Kimpel, N. Kosinov, E.J.M. Hensen, Boosting CO_2 hydrogenation via size-dependent metal–support interactions in cobalt/ceria-based catalysts, Nat. Catal. 3 (2020) 526–533, https://doi.org/10.1038/s41929-020-0459-4.
[5] S. Kattel, P.J. Ramirez, J.G. Chen, J.A. Rodriguez, P. Liu, Active sites for CO_2 hydrogenation to methanol on Cu/ZnO catalysts, Science 355 (2017) 1296–1299, https://doi.org/10.1126/science.aal3573.
[6] S. Kuld, M. Thorhauge, H. Falsig, C.F. Elkjaer, S. Helveg, I. Chorkendorff, J. Sehested, Quantifying the promotion of Cu catalysts by ZnO for methanol synthesis, Science 352 (2016) 969–974, https://doi.org/10.1126/science.aaf0718.
[7] J. Hu, L. Yu, J. Deng, Y. Wang, K. Cheng, C. Ma, Q. Zhang, W. Wen, S. Yu, Y. Pan, J. Yang, H. Ma, F. Qi, Y. Wang, Y. Zheng, M. Chen, R. Huang, S. Zhang, Z. Zhao, J. Mao, X. Meng, Q. Ji, G. Hou, X. Han, X. Bao, Y. Wang, D. Deng, Sulfur vacancy-rich MoS_2 as a catalyst for the hydrogenation of CO_2 to methanol, Nat. Catal. 4 (2021) 242–250, https://doi.org/10.1038/s41929-021-00584-3.
[8] X. Zhang, J.-X. Liu, B. Zijlstra, I.A.W. Filot, Z. Zhou, S. Sun, E.J.M. Hensen, Optimum Cu nanoparticle catalysts for CO_2 hydrogenation towards methanol, Nano Energy 43 (2018) 200–209, https://doi.org/10.1016/j.nanoen.2017.11.021.
[9] S. Zhang, Z. Wu, X. Liu, Z. Shao, L. Xia, L. Zhong, H. Wang, Y. Sun, Tuning the interaction between Na and Co_2C to promote selective CO_2 hydrogenation to ethanol, Appl. Catal. B 293 (2021), 120207, https://doi.org/10.1016/j.apcatb.2021.120207.
[10] K. Mori, T. Sano, H. Kobayashi, H. Yamashita, Surface engineering of a supported PdAg catalyst for hydrogenation of CO_2 to formic acid: Elucidating the active Pd atoms in alloy nanoparticles, J. Am. Chem. Soc. 140 (2018) 8902–8909, https://doi.org/10.1021/jacs.8b04852.
[11] F. Frusteri, G. Bonura, C. Cannilla, G. Drago Ferrante, A. Aloise, E. Catizzone, M. Migliori, G. Giordano, Stepwise tuning of metal-oxide and acid sites of CuZnZr-MFI hybrid catalysts for the direct DME synthesis by CO_2 hydrogenation, Appl. Catal. B 176–177 (2015) 522–531, https://doi.org/10.1016/j.apcatb.2015.04.032.
[12] P. Gao, S. Li, X. Bu, S. Dang, Z. Liu, H. Wang, L. Zhong, M. Qiu, C. Yang, J. Cai, W. Wei, Y. Sun, Direct conversion of CO_2 into liquid fuels with high selectivity over a bifunctional catalyst, Nat. Chem. 9 (2017) 1019–1024, https://doi.org/10.1038/nchem.2794.
[13] C.G. Visconti, M. Martinelli, L. Falbo, A. Infantes-Molina, L. Lietti, P. Forzatti, G. Iaquaniello, E. Palo, B. Picutti, F. Brignoli, CO_2 hydrogenation to lower olefins on a high surface area K-promoted bulk Fe-catalyst, Appl. Catal. B 200 (2017) 530–542, https://doi.org/10.1016/j.apcatb.2016.07.047.

[14] Y. Ni, Z. Chen, Y. Fu, Y. Liu, W. Zhu, Z. Liu, Selective conversion of CO_2 and H_2 into aromatics, Nat. Commun. 9 (2018) 3457, https://doi.org/10.1038/s41467-018-05880-4.

[15] A. Modak, P. Bhanja, S. Dutta, B. Chowdhury, A. Bhaumik, Catalytic reduction of CO_2 into fuels and fine chemicals, Green. Chem. 22 (2020) 4002–4033, https://doi.org/10.1039/d0gc01092h.

[16] S. Zander, E.L. Kunkes, M.E. Schuster, J. Schumann, G. Weinberg, D. Teschner, N. Jacobsen, R. Schlogl, M. Behrens, The role of the oxide component in the development of copper composite catalysts for methanol synthesis, Angew. Chem. Int. Ed. 52 (2013) 6536–6540, https://doi.org/10.1002/anie.201301419.

[17] J. Wang, G. Li, Z. Li, C. Tang, Z. Feng, H. An, H. Liu, T. Liu, C. Li, A highly selective and stable ZnO-ZrO_2 solid solution catalyst for CO_2 hydrogenation to methanol, Sci. Adv. 3 (2017), e1701290, https://doi.org/10.1126/sciadv.1701290.

[18] O. Martin, A.J. Martin, C. Mondelli, S. Mitchell, T.F. Segawa, R. Hauert, C. Drouilly, D. Curulla-Ferre, J. Perez-Ramirez, Indium oxide as a superior catalyst for methanol synthesis by CO_2 hydrogenation, Angew. Chem. Int. Ed. 55 (2016) 6261–6265, https://doi.org/10.1002/anie.201600943.

[19] C. Meng, G. Zhao, X.R. Shi, P. Chen, Y. Liu, Y. Lu, Oxygen-deficient metal oxides supported nano-intermetallic $InNi_3C_{0.5}$ toward efficient CO_2 hydrogenation to methanol, Sci. Adv. 7 (2021) eabi6012, https://doi.org/10.1126/sciadv.abi6012.

[20] Z. Shi, Q. Tan, C. Tian, Y. Pan, X. Sun, J. Zhang, D. Wu, CO_2 hydrogenation to methanol over Cu-In intermetallic catalysts: Effect of reduction temperature, J. Catal. 379 (2019) 78–89, https://doi.org/10.1016/j.jcat.2019.09.024.

[21] E.S. Gutterod, S.H. Pulumati, G. Kaur, A. Lazzarini, B.G. Solemsli, A.E. Gunnaes, C. Ahoba-Sam, M.E. Kalyva, J.A. Sannes, S. Svelle, E. Skulason, A. Nova, U. Olsbye, Influence of defects and H_2O on the hydrogenation of CO_2 to methanol over Pt nanoparticles in UiO-67 Metal-Organic Framework, J. Am. Chem. Soc. 142 (2020) 17105–17118, https://doi.org/10.1021/jacs.0c07153.

[22] S. Posada-Perez, P.J. Ramirez, J. Evans, F. Vines, P. Liu, F. Illas, J.A. Rodriguez, Highly active Au/delta-MoC and Cu/delta-MoC catalysts for the conversion of CO_2: The metal/C ratio as a key factor defining activity, selectivity, and stability, J. Am. Chem. Soc. 138 (2016) 8269–8278, https://doi.org/10.1021/jacs.6b04529.

[23] Y. Wang, S. Kattel, W. Gao, K. Li, P. Liu, J.G. Chen, H. Wang, Exploring the ternary interactions in Cu-ZnO-ZrO_2 catalysts for efficient CO_2 hydrogenation to methanol, Nat. Commun. 10 (2019) 1166, https://doi.org/10.1038/s41467-019-09072-6.

[24] M. Huš, V.D.B.C. Dasireddy, N. Strah Štefančič, B. Likozar, Mechanism, kinetics and thermodynamics of carbon dioxide hydrogenation to methanol on Cu/$ZnAl_2O_4$ spinel-type heterogeneous catalysts, Appl. Catal. B 207 (2017) 267–278, https://doi.org/10.1016/j.apcatb.2017.01.077.

[25] B. Liang, J. Ma, X. Su, C. Yang, H. Duan, H. Zhou, S. Deng, L. Li, Y. Huang, Investigation on deactivation of Cu/ZnO/Al_2O_3 Catalyst for CO_2 Hydrogenation to Methanol, Ind. Eng. Chem. Res. 58 (2019) 9030–9037, https://doi.org/10.1021/acs.iecr.9b01546.

[26] X. Zhang, G. Zhang, W. Liu, F. Yuan, J. Wang, J. Zhu, X. Jiang, A. Zhang, F. Ding, C. Song, X. Guo, Reaction-driven surface reconstruction of $ZnAl_2O_4$ boosts the methanol selectivity in CO_2 catalytic hydrogenation, Appl. Catal. B 284 (2021), 119700, https://doi.org/10.1016/j.apcatb.2020.119700.

[27] M.S. Frei, C. Mondelli, R. García-Muelas, K.S. Kley, B. Puértolas, N. López, O. V. Safonova, J.A. Stewart, D. Curulla Ferré, J. Pérez-Ramírez, Atomic-scale engineering of indium oxide promotion by palladium for methanol production via CO_2 hydrogenation, Nat. Commun. 10 (2019) 3377, https://doi.org/10.1038/s41467-019-11349-9.

[28] Y. Lu, T. Liu, Y.-C. Huang, L. Zhou, Y. Li, W. Chen, L. Yang, B. Zhou, Y. Wu, Z. Kong, Z. Huang, Y. Li, C.-L. Dong, S. Wang, Y. Zou, Integrated catalytic sites for highly efficient electrochemical oxidation of the aldehyde and hydroxyl groups in 5-hydroxymethylfurfural, ACS Catal. 12 (2022) 4242–4251, https://doi.org/10.1021/acscatal.2c00174.

[29] H. Nguyen-Phu, E.W. Shin, Disordered structure of $ZnAl_2O_4$ phase and the formation of a Zn NCO complex in ZnAl mixed oxide catalysts for glycerol carbonylation with urea, J. Catal. 373 (2019) 147–160, https://doi.org/10.1016/j.jcat.2019.03.043.

[30] L. Liu, Y. Lin, Y. Hu, Z. Lin, S. Lin, M. Du, L. Zhang, X.-h Zhang, J. Lin, Z. Zhang, H. Xiong, S. Wang, B. Ge, S. Wan, Y. Wang, $ZnAl_2O_4$ spinel-supported $PdZn_\beta$ catalyst with parts per million Pd for methanol steam reforming, ACS Catal. 12 (2022) 2714–2721, https://doi.org/10.1021/acscatal.1c04922.

[31] J. Okal, M. Zawadzki, Combustion of propane over novel zinc aluminate-supported ruthenium catalysts, Appl. Catal. B 105 (2011) 182–190, https://doi.org/10.1016/j.apcatb.2011.04.013.

[32] F.L. Peltier, P. Chaumette, J. Saussey, M.M. Bettahar, J.C. Lavalley, In situ FT-IR and kinetic study of methanol synthesis from CO_2/H_2 over $ZnAl_2O_4$ and Cu–$ZnAl_2O_4$ catalysts, J. Mol. Catal. A: Chem. 132 (1998) 91–100, https://doi.org/10.1016/S1381-1169(97)00235-5.

[33] M. Behrens, S. Zander, P. Kurr, N. Jacobsen, J. Senker, G. Koch, T. Ressler, R. W. Fischer, R. Schlogl, Performance improvement of nanocatalysts by promoter-induced defects in the support material: methanol synthesis over Cu/ZnO: Al, J. Am. Chem. Soc. 135 (2013) 6061–6068, https://doi.org/10.1021/ja310456f.

[34] C. Dong, Z. Qu, Y. Qin, Q. Fu, H. Sun, X. Duan, Revealing the highly catalytic performance of spinel $CoMn_2O_4$ for toluene oxidation: Involvement and replenishment of oxygen species using in situ designed-TP techniques, ACS Catal. 9 (2019) 6698–6710, https://doi.org/10.1021/acscatal.9b01324.

[35] N. Li, W. Wang, L. Song, H. Wang, Q. Fu, Z. Qu, CO_2 hydrogenation to methanol promoted by Cu and metastable tetragonal $Ce_xZr_yO_z$ interface, J. Energy Chem. 68 (2022) 771–779, https://doi.org/10.1016/j.jechem.2021.12.053.

[36] W. Wang, Z. Qu, L. Song, Q. Fu, Probing into the multifunctional role of copper species and reaction pathway on copper-cerium-zirconium catalysts for CO_2 hydrogenation to methanol using high pressure in situ DRIFTS, J. Catal. 382 (2020) 129–140, https://doi.org/10.1016/j.jcat.2019.12.022.

[37] R. Ianoş, S. Borcănescu, R. Lazău, Large surface area $ZnAl_2O_4$ powders prepared by a modified combustion technique, Chem. Eng. J. 240 (2014) 260–263, https://doi.org/10.1016/j.cej.2013.11.082.

[38] P. Sripada, J. Kimpton, A. Barlow, T. Williams, S. Kandasamy, S. Bhattacharya, Investigating the dynamic structural changes on Cu/CeO_2 catalysts observed during CO_2 hydrogenation, J. Catal. 381 (2020) 415–426, https://doi.org/10.1016/j.jcat.2019.11.017.

[39] J. Zhong, X. Yang, Z. Wu, B. Liang, Y. Huang, T. Zhang, State of the art and perspectives in heterogeneous catalysis of CO_2 hydrogenation to methanol, Chem. Soc. Rev. 49 (2020) 1385–1413, https://doi.org/10.1039/c9cs00614a.

[40] J. Yu, M. Yang, J. Zhang, Q. Ge, A. Zimina, T. Pruessmann, L. Zheng, J.-D. Grunwaldt, J. Sun, Stabilizing Cu^+ in Cu/SiO_2 Catalysts with a shattuckite-like structure boosts CO_2 hydrogenation into methanol, ACS Catal. 10 (2020) 14694–14706, https://doi.org/10.1021/acscatal.0c04371.

[41] Z. He, H. Lin, P. He, Y. Yuan, Effect of boric oxide doping on the stability and activity of a Cu-SiO_2 catalyst for vapor-phase hydrogenation of dimethyl oxalate to ethylene glycol, J. Catal. 277 (2011) 54–63, https://doi.org/10.1016/j.jcat.2010.10.010.

[42] W. Di, J. Cheng, S. Tian, J. Li, J. Chen, Q. Sun, Synthesis and characterization of supported copper phyllosilicate catalysts for acetic ester hydrogenation to ethanol, Appl. Catal., A 510 (2016) 244–259, https://doi.org/10.1016/j.apcata.2015.10.026.

[43] K. Hadjiivanov, H. Knözinger, FTIR study of CO and NO adsorption and coadsorption on a Cu/SiO_2 catalyst: probing the oxidation state of copper, Phys. Chem. Chem. Phys. 3 (2001) 1132–1137, https://doi.org/10.1039/b009649k.

[44] F. You, J. Wan, J. Qi, D. Mao, N. Yang, Q. Zhang, L. Gu, D. Wang, Lattice distortion in hollow multi-shelled structures for efficient visible-light CO_2 reduction with a SnS_2 /SnO_2 junction, Angew. Chem. Int. Ed. 59 (2020) 721–724, https://doi.org/10.1002/anie.201912069.

[45] J. Yang, X. Zhu, Q. Yu, M. He, W. Zhang, Z. Mo, J. Yuan, Y. She, H. Xu, H. Li, Multidimensional In_2O_3/In_2S_3 heterojunction with lattice distortion for CO_2 photoconversion, Chin. J. Catal. 43 (2022) 1286–1294, https://doi.org/10.1016/s1872-2067(21)63954-2.

[46] H. Yan, S. Yao, W. Liang, S. Zhao, X. Jin, X. Feng, Y. Liu, X. Chen, C. Yang, Ni–Co oxide catalysts with lattice distortions for enhanced oxidation of glycerol to glyceric acid, J. Catal. 381 (2020) 248–260, https://doi.org/10.1016/j.jcat.2019.11.001.

[47] Y. Zhu, Y. Zhu, G. Ding, S. Zhu, H. Zheng, Y. Li, Highly selective synthesis of ethylene glycol and ethanol via hydrogenation of dimethyl oxalate on Cu catalysts: Influence of support, Appl. Catal., A 468 (2013) 296–304, https://doi.org/10.1016/j.apcata.2013.09.019.

[48] J. Agrell, Production of hydrogen from methanol over Cu/ZnO catalysts promoted by ZrO_2 and Al_2O_3, J. Catal. 219 (2003) 389–403, https://doi.org/10.1016/s0021-9517(03)00221-5.

[49] X. Dong, F. Li, N. Zhao, F. Xiao, J. Wang, Y. Tan, CO_2 hydrogenation to methanol over Cu/ZnO/ZrO_2 catalysts prepared by precipitation-reduction method, Appl. Catal. B 191 (2016) 8–17, https://doi.org/10.1016/j.apcatb.2016.03.014.

[50] G. Pacchioni, Oxygen vacancy: the invisible agent on oxide surfaces, Chemphyschem 4 (2003) 1041–1047, https://doi.org/10.1002/cphc.200300835.

[51] Y. Hu, Y. Pan, Z. Wang, T. Lin, Y. Gao, B. Luo, H. Hu, F. Fan, G. Liu, L. Wang, Lattice distortion induced internal electric field in TiO_2 photoelectrode for efficient charge separation and transfer, Nat. Commun. 11 (2020) 2129, https://doi.org/10.1038/s41467-020-15993-4.

[52] J. Ni, W. Leng, J. Mao, J. Wang, J. Lin, D. Jiang, X. Li, Tuning electron density of metal nickel by support defects in Ni/ZrO_2 for selective hydrogenation of fatty acids to alkanes and alcohols, Appl. Catal. B 253 (2019) 170–178, https://doi.org/10.1016/j.apcatb.2019.04.043.

[53] C.P. Jiménez-Gómez, J.A. Cecilia, D. Durán-Martín, R. Moreno-Tost, J. Santamaría-González, J. Mérida-Robles, R. Mariscal, P. Maireles-Torres, Gas-phase hydrogenation of furfural to furfuryl alcohol over Cu/ZnO catalysts, J. Catal. 336 (2016) 107–115, https://doi.org/10.1016/j.jcat.2016.01.012.

[54] C. Huang, J. Wen, Y. Sun, M. Zhang, Y. Bao, Y. Zhang, L. Liang, M. Fu, J. Wu, D. Ye, L. Chen, CO_2 hydrogenation to methanol over Cu/ZnO plate model catalyst: effects of reducing gas induced Cu nanoparticle morphology, Chem. Eng. J. 374 (2019) 221–230, https://doi.org/10.1016/j.cej.2019.05.123.

[55] Y. Sun, C. Huang, L. Chen, Y. Zhang, M. Fu, J. Wu, D. Ye, Active site structure study of Cu/Plate ZnO model catalysts for CO_2 hydrogenation to methanol under the real reaction conditions, J. CO_2 Util. 37 (2020) 55–64, https://doi.org/10.1016/j.jcou.2019.11.029.

[56] X. Jiang, X. Nie, X. Wang, H. Wang, N. Koizumi, Y. Chen, X. Guo, C. Song, Origin of Pd-Cu bimetallic effect for synergetic promotion of methanol formation from CO_2 hydrogenation, J. Catal. 369 (2019) 21–32, https://doi.org/10.1016/j.jcat.2018.10.001.

[57] Y. Hartadi, D. Widmann, R.J. Behm, Methanol formation by CO_2 hydrogenation on Au/ZnO catalysts - Effect of total pressure and influence of CO on the reaction characteristics, J. Catal. 333 (2016) 238–250, https://doi.org/10.1016/j.jcat.2015.11.002.

[58] K. Lorber, J. Zavašnik, I. Arčon, M. Huš, J. Teržan, B. Likozar, P. Djinović, CO_2 activation over nanoshaped CeO_2 decorated with nickel for low-temperature methane dry reforming, ACS Appl. Mater. Interfaces 14 (2022) 31862–31878, https://doi.org/10.1021/acsami.2c05221.